Journal of Mathematical Chemistry (2024) 62:535–554
https://doi.org/10.1007/s10910-023-01553-w

ORIGINAL PAPER

# Optimized derivative fast Fourier transform with high resolution and low noise from encoded time signals: Ovarian NMR spectroscopy

**Dževad Belkić**[1,2] · **Karen Belkić**[1,2,3,4]

Received: 1 November 2023 / Accepted: 10 November 2023 / Published online: 8 December 2023


## Abstract

The unfiltered derivative fast Fourier transform (dFFT) of degrees higher than two fails flagrantly for encoded time signals. These data are always dominated by noise at larger times of encodings. Such a breakdown is due to processing the unweighted product of the time signal and the time power function. The latter is generated by the frequency derivative operator applied to the fast Fourier transform (FFT). As a result, the unfiltered dFFT cannot separate the overlapped resonances and it dramatically decreases signal-to-noise ratio (SNR) relative to the FFT. This problem is solved by a derivative-adapted optimization with the properly attenuated filters. The ensuing optimized dFFT achieves the long sought simultaneous enhancement of both resolution and SNR. It uncovers the genuine resonances hidden within overlapping peaks to enable quantitative interpretations. It does not impose any model on the input time signals nor on the output lineshape in the spectra. It is computationally expedient as it uses the Cooley-Tukey fast algorithm. The present applications deal with time signals encoded by in vitro NMR spectroscopy from human malignant ovarian cyst fluid. A remarkably successful performance of the optimized dFFT is demonstrated for reconstructed spectra of potentially added value in clinical decision-making.

✉ Dževad Belkić
Dzevad.Belkic@ki.se

Karen Belkić
Karen.Belkic@ki.se

1 Department of Oncology-Pathology, Karolinska Institute, P.O. Box 260, 171 76 Stockholm, Sweden

2 Radiation Physics and Nuclear Medicine, Karolinska University Hospital, P.O. Box 260, 171 76 Stockholm, Sweden

3 School of Community and Global Health, Claremont Graduate University, Claremont, CA 91711, USA

4 Institute for Health Promotion and Disease Prevention Research, University of Southern California School of Medicine, Alhambra, CA 91803-8800, USA

**Keywords** Optimized derivative fast Fourier transform · Resolution enhancement · Noise reduction · NMR spectroscopy

## 1 Introduction

The large field of signal processing [1–4] encompasses several spectroscopies for versatile applications ranging from basic through applied sciences to life sciences, as well as to technologies and industries. Also included here are the multifaceted aspects of nuclear magnetic resonance (NMR) spectroscopy [5, 6], alternatively called magnetic resonance spectroscopy (MRS) in medicine [7–14]. In many branches relying upon signal processing, the fast Fourier transform (FFT) [1–4] with or without some weight/apodization functions (filters) is abundantly applied. This is not deterred by the well-documented numerous limitations of the FFT, particularly for measured/encoded time signals. In MRS, time signals are synonymously called the free induction decay (FID) data, that are used as discretized/digitized curves.

The two main pitfalls of the FFT are its low resolution in frequency $\nu$ and poor signal-to-noise ratio (SNR). In principle, both failures should be rectifiable by the unweighted/unfiltered derivative fast Fourier transform (dFFT), which employs the product of the time power function (monomial) and the input FID. They are not for encoded FIDs, as has thoroughly been illustrated for MRS [15–29]. From here and on, this unfiltered (unweighted, unsmoothed) dFFT will be referred to as the unoptimized dFFT.

In the unoptimized dFFT for encoded FIDs, denoted by $c(t)$ in their continuous/analog representation, resolution and SNR are catastrophically deteriorated for increased derivative orders (say $m$), starting already with $m > 2$. The reason is that this estimator processes the unfiltered function $t^m c(t)$. Here, the power function, i.e. the monomial $t^m$ ($m = 1, 2, 3, ...$), comes from applying the frequency-dependent derivative operator $(\mathrm{d}/\mathrm{d}\nu)^m$ to the exponential $\mathrm{e}^{-2\pi i \nu t}$, contained in the finite $\nu-$dependent Fourier integral over time $t \in [0, T]$. Constant $T$ is the total acquisition time of the FID (i.e. the total duration of the time signal). In encoded FIDs, noise prevails at larger values of $t$. Therefore, in the unoptimized dFFT, the monomial $t^m$ amplies noise at larger $t$. This worsens both resolution and SNR with augmenting derivative orders $m$.

Advantageously, however, the FFT itself does not assume any particular form of the FIDs nor of the spectral lineshapes. Such a model-independence feature is automatically preserved by all the variants of the Fourier-based derivative estimations. Directly or indirectly, the other existing processors describe the FID and/or the spectral lineshapes by various mathematical expressions (models). For the FIDs, these are usually some linear combinations of complex damped exponentials, eventually multiplied by real decreasing Gaussians. Likewise, for spectral profiles, often employed models are the Lorentzian or Gaussian lineshapes (or their Voigt-type combinations) [10, 11].

For synthesized noiseless FIDs, the unoptimized dFFT works as per the expectations from the principles of derivative estimations. It successfully unravels the true components, weak and strong alike. They are folded in the overlapped resonances from the corresponding FFT spectrum. This is attributed solely to the monomial $t^m$ which, by acting as an unfolding operator, is capable of peering into the hidden struc-

ture of a total shape spectrum (envelope). The power function $t^m$, multiplying $c(t)$, amplifies all the peaks in the corresponding spectrum from the unoptimized dFFT, including the minuscule structures. Such an outcome is a bonus for idealized noise-free FIDs. However, these are not encountered in the real-world problems. Hence, it is noise (synthesized or measured) that blocks the drive of the unoptimized dFFT to the hoped-for success.

For encoded noise-contaminated FIDs, it would then be of great importance to have the Fourier-conceived derivative estimation, which preserves the mentioned model-independence, while applying the Cooley-Tukey fast computations [1] to simultaneously enhance resolution and SNR. This is achievable utilizing an efficient optimization with an analytical/closed expression for a derivative-adapted damping/attenuating filter [29]. The resulting processor, called the optimized dFFT [29], contains a single parameter, which is adapted to the running derivative order $m$ and is simultaneously tailored to the SNR of the input FID data. This twofold feature is provided by the adaptive power-exponential filter (APEF) or the adaptive power-Gaussian filter (APGF) that both decrease with augmentation of time $t$.

The optimized and unoptimized variants of the dFFT, alongside the FFT, are presently applied to the FIDs encoded by in vitro MRS with water suppression at a 600 MHz (14.1 T) Bruker spectrometer from human cancerous ovarian cyst fluid [30]. In a part of the aliphatic region, we focus on two narrow chemical shift bands containing the recognized and potential cancer biomarkers, the choline compounds and the citrate metabolites, respectively.

It is shown that the optimized dFFT for encoded FIDs can successfully solve the mentioned two major problems in signal processing, while emerging as a high-resolution processor with maximal SNR. This is accomplished by gradually increasing the derivative order ($1 \leq m \leq 5$). The obtained steadily stabilized lineshapes, amenable to autonomous quantitative interpretations, are deemed to be of notable practical utility in tumor diagnostics by in vitro as well as by in vivo MRS not only for the ovary, but also for other human organs. Moreover, the expounded strategy of the optimized derivative Fourier signal processing is anticipated to find useful applications in vastly different fields across interdisciplinary spectroscopy-based explorations.

## 2 Theory

For the given FID or time signal $\{c_n\}$ $(0 \leq n \leq N-1)$ of total length $N = 2^\ell$ $(\ell = 1, 2, 3, ...)$ and duration $T$, sampled at the rate $\tau$, the optimized dFFT from Ref. [29] is obtained by applying the Cooley-Tukey algorithm [1] to the complex-valued sequence:

$$\text{Optimized dFFT}: \quad \mathrm{D}_m\mathrm{FFT} = \frac{1}{N}\sum_{n=0}^{N-1} \mathrm{O}_{n,m} c_n W_k^n, \tag{1}$$

where $W_k = \mathrm{e}^{-2\pi i k/N}$ $(0 \leq k \leq N-1)$. Here, $\mathrm{D}_m\mathrm{FFT}$ is, in fact, $\mathrm{D}_{k,m}\mathrm{FFT}$ $(0 \leq k \leq N-1)$, but for brevity the subscript $k$ is dropped from the lhs of Eq. (1) and this convention will be used throughout.

The quantity $O_{n,m}$ in (1) is the object function of the optimization. It is a derivative-adapted attenuating function. The highly effective two forms of $O_{n,m}$ have recently been implemented [29]. One is the adaptive power-exponential filter, the APEF:

$$\text{APEF}: \ O_{n,m} = (-2\pi i n\tau)^m e^{-\lambda_E(m,\alpha)n\tau}, \tag{2}$$

$$\lambda_E(m,\alpha) = \frac{m}{T} ln(T e^{\alpha}). \tag{3}$$

The other is the adaptive power-Gaussian filter, the APGF:

$$\text{APGF}: \ O_{n,m} = (-2\pi i n\tau)^m e^{-\lambda_G(m,\beta)(n\tau)^2}, \tag{4}$$

$$\lambda_G(m,\beta) = \frac{m}{T^2} ln(T e^{\beta}). \tag{5}$$

In the derivative-adapted attenuation terms $\lambda_E(m,\alpha) > 0$ or $\lambda_G(m,\beta) > 0$, the single parameter $\alpha > 0$ or $\beta > 0$, respectively, mimics the SNR of the original FID by assessing the decay of the FID transients to zero at the end of encodings, i.e. at $t = T$ ($T = N\tau$). Encoded FIDs are de facto truncated because their total acquisition times are necessarily finite ($T < \infty$). This is equivalent to multiplying an FID by a Heaviside step-function which, in turn, yields the spectral distortions (Gibbs ringing, flanking wiggles) around the reconstructed resonances.

In e.g. the APEF, constant $\alpha$ is a measure of the damping rate $T/T_2^\star$ in the longest-lasting transient envelope $A(0)e^{-t/T_2^\star}$ of $c(t)$ at $t = T$. Here, $A(0)$ is the FID initial intensity at the onset of encodings ($t = 0$) and $T_2^\star$ is the transverse relaxation time. Thus, e.g. a choice $\alpha = 3$ in the APEF would characterize an FID transient whose intensity $A(T)$ at the end of encodings ($t = T$) decayed to about 5% ($e^{-3} \approx 0.4598$) of $A(0)$. Such a value of $\alpha$ optimizes the damping parameter $\lambda_E(m,\alpha)$ so that it duly reflects the SNR of the FID directly through its decay to the noise level of encodings. The implication is that with the APEF in the optimized dFFT, the mentioned Gibbs lineshape distortions from the FID truncation will be smaller than the noise in the spectrum.

Formula (1) also provides the nonderivative FFT and the unoptimized dFFT, both in their unfiltered versions, if we set $\lambda_E(m,\alpha) = 0$ in (2) or $\lambda_G(m,\beta) = 0$ in (4):

$$\text{FFT} = \frac{1}{N}\sum_{n=0}^{N-1} c_n W_k^n, \quad 0 \le k \le N-1, \tag{6}$$

$$\text{Unoptimized dFFT}: \quad D_m\text{FFT} = \frac{1}{N}\sum_{n=0}^{N-1} (-2\pi i n\tau)^m c_n W_k^n, \tag{7}$$

respectively. For simplicity, both variants of the dFFT, the optimized (1) and unoptimized (7) are denoted by the same symbol $D_m$FFT, which includes the FFT as $D_0$FFT = FFT. The context will indicate to which of these two spectral lineshapes the given remark is made. The corresponding spectra will be distinguished in the plots with the markings "Optimized" and "Unoptimized" or "Filtering" and "No Filtering".

As elaborated in Refs. [15–17], for visualizations of spectra, the most convenient is the phase-insensitive, positive-definite magnitude mode $|D_m FFT|$ ($m = 0, 1, 2, ...$) of complex $D_m FFT$ ($m \geq 0$), where $|D_0 FFT| = |FFT|$.

Moreover, because of the peak width narrowing and peak height enhancing with rising $m$, monitoring the lineshape profile developments for the successive derivative orders $m > 0$ is conveniently facilitated by using the normalized magnitude spectra $|D_m FFT|_N$ defined as:

$$|D_m FFT|_N = |D_m FFT| \frac{|FFT|^{max}}{|D_m FFT|^{max}} \quad (m = 1, 2, ...), \tag{8}$$

$$|D_m FFT|^{max} = \max |D_m FFT| \quad (m = 0, 1, 2, ...). \tag{9}$$

Observe that the nonderivative FFT ($m = 0$), as $|FFT|^{max}$, is included in (9). Of course, the nonderivative spectrum |FFT| itself is not normalized[1].

The implementation of the optimized dFFT in Ref. [29] has been illustrated for the FIDs encoded by in vitro MRS at low (1.5T) and high (14.1T) magnetic fields.[2] The latter FIDs encoded in Ref. [30] are also employed in the current study, which emphasizes two narrow chemical shift bands in a part of the aliphatic region containing the recognized and potential cancer biomarkers, the choline compounds and the citrate quartet, respectively.

## 3 Results and discussion

Versatile possibilities to noninvasively monitor metabolic processes in patients were the prime reason for the physician interest in MRS. To that end, one of the key goals is to distinguish normal from diseased tissues and/or biofluids of patients. To be useful in this regard, MRS information, extractable from resonances in spectra, reconstructed with encoded FIDs, must be reliable, quantifiable and metabolically distinct to a sufficient extent to differentiate normal from diseased organs or samples. In cancer medicine, MRS findings ought to be clearly different for cancerous and benign specimens. Here, one of the main tasks of MRS is to identify metabolites that could be considered as cancer biomarkers. Such identifications by MRS should be statistically significant in face of the variability of samples and despite adverse effects of some other factors that can impede and complicate the analysis.

One such factor is the presence of ubiquitous overlapping resonances in spectra that most severely plague the FFT and preclude the clinically reliable identification of cancer biomarkers. It is here that the optimized dFFT comes to the rescue, as has recently been shown in Ref. [29] and will also be further explored in the current study.

[1] Note that Eq. (4) in Ref. [29] has been misprinted as $|D_m S| = |S|^{max} / |D_m S|^{max}$ instead of:

$$|D_m S|_N = |D_m S| \frac{|S|^{max}}{|D_m S|^{max}} \quad (m = 1, 2, ...)$$

which is the present Eq. (8) rewritten in the notation of Ref. [29], where S=FFT.

[2] When derivative estimations are applied to MRS, the term derivative magnetic resonance spectroscopy (dMRS) seems to be more appropriate.

For some forty patients, using a Bruker high-resolution spectrometer, the authors of Ref. [30] have encoded the FIDs from samples of ovarian cyst fluid. The plan was to see whether MRS could be employed to differentiate between the samples that were independently diagnosed as benign and malignant for twenty-eight and twelve patients, respectively. This was indeed feasible for a number of metabolites, as elaborated in Ref. [30]. The authors of Ref. [30] have kindly given to us two of their FIDs encoded from benign and malignant samples. The latter sample (serous cystadenocarcinoma) is the subject of the present analysis.

For MRS of the ovary, among the recognized cancer biomarkers, one finds the choline compounds that are more abundant in malignant than in benign lesions. However, for the same organ, the concentration levels of citrates are more elevated in benign than in cancerous pathologies. Therefore, to enlarge the diagnostic window, the citrate metabolites could be considered as potential cancer biomarkers for ovarian cyst fluid, according to Refs. [25, 30, 36]. The citrate metabolites are recognized cancer biomarkers for the prostate. Concentration levels of these molecules are low in cancerous prostate, but high in normal prostate and in benign prostatic hypertrophy [14, 32, 37–43].

The list of potential cancer biomarkers for the ovary could be extended to encompass also a number of other molecules whose resonances at $0.9-1.6$ ppm (parts per million) are significantly stronger in malignant relative to benign samples of ovarian cyst fluid [25, 30]. These are multiplets (doublet d, triplet t) of alanine Ala(d), threonine Thr(d), $\beta-$hydroxylbutyric acid $\beta-$HB(d) or 3-HB(d), leucine Leu(d,t) and isoleucine Iso(d,t). Within this latter chemical shift interval of length of only 0.7 ppm also lies the lactate doublet Lac(d) at about 1.41 ppm, as a recognized cancer biomarker for the ovary.

We will now illustrate the optimized dFFT for processing an averaged FID from 128 transient time signals encoded with water suppression by in vitro proton MRS. As stated, encodings were made at a Bruker spectrometer from a sample of human malignant ovarian cyst fluid (serous cystadenocarcinoma) dissolved in $D_2O$ [30]. These data entail the following specific encoding parameters: the Larmor frequency $\nu_L = 600\,\text{MHz}$ ($B_0 \approx 14.1\text{T}$), the total signal length $N = 16384$, the repetition time TR=1200 ms, the echo time TE=30 ms, the bandwidth BW=6667 Hz, the sampling time $\tau = 1/\text{BW} \approx 0.15$ ms, the total acquisition time $T = N\tau = 2.46$s and the number of excitations NEX=128 (the number of the measured FID transients).

Trimethylsilyl-2-2-3-3-tetradeuteropropionic (TSP) acid was added to the sample for a twofold internal referencing [30]. First, the locations of all the other resonance frequencies on the chemical shift axis are counted from the center ($\nu = 0.0$ ppm) of the $CH_3$ singlet of TSP. Second, for the resonances other than this latter reference peak, the reconstructed concentrations of the assigned metabolites are expressed as the percentage of the known TSP concentration in the biophysical units, micro-mol per gram per weight ($\mu$M/g). In quantifying the identified resonances, the real part of the computed complex FFT spectra in Ref. [30] was manually corrected for the phase and background to have approximately positive-definite lineshapes.

Further, the Lorentzian lineshape model was employed in Ref. [30] for fitting the spectral structures from the FFT 'absorptive' spectra. Therein, the widths of the

detected peaks were taken to be about 1.0 Hz throughout the Nyquist range.[3] The extracted peak areas were related to the concentrations of the metabolites assigned to the quantified resonances. The concentrations of only 12 quantified metabolites were reported [30]. The reason for not obtaining the concentrations of many other remaining resonances was attributed in Ref. [30] to the "spectral crowding". This latter term is occasionally used to refer to some heavy overlaps of tightly packed resonances [31–35].

Using the averaged FID from these time-domain acquired transients [30], all the presently reconstructed Fourier-based spectra in the nonderivative FFT, as well as in the unoptimized and optimized derivative dFFT will be graphed in the magnitude mode. In the magnitude mode, $|\mathrm{D}_m\mathrm{FFT}|$, the sidelobes around resonances for $m \geq 1$ are suppressed by interference between the real and imaginary parts, $\mathrm{Re}(\mathrm{D}_m\mathrm{FFT})$ and $\mathrm{Im}(\mathrm{D}_m\mathrm{FFT})$, respectively. This is yet another advantage of magnitudes $|\mathrm{D}_m\mathrm{FFT}|$ over the 'absorptions' $\mathrm{Re}(\mathrm{D}_m\mathrm{FFT})$, given that in the latter spectra, the sidelobes are intensified for increasing $m \geq 1$ and, as such, could be misinterpreted as the physical resonances. In the normalized derivative spectra $|\mathrm{D}_m\mathrm{FFT}|_\mathrm{N}$ ($m = 1, 2, 3, ...$) to be displayed, normalization is made to one of the resonance peaks in the analyzed chemical shift band.

Our perspective is to try to separate the overlapped resonances by extracting the components from the $J-$coupled multiplets. The salient illustrations will be given with the emphasis on the citrate quartet Cit(q) and the choline compounds. The resonances of these metabolites are located in a tight chemical shift range 2.80−3.29 ppm, which extends over merely 0.49 ppm. For an easier follow-up, the spectral lineshapes in the reported figures are color-coded in black, blue and red lines for the nonderivative FFT, the optimized dFFT and the unoptimized dFFT, respectively.

### 3.1 Citrate quartet (2.80−3.05 ppm)

Figure 1 shows the Fourier-based reconstructions of spectra in the chemical shift band containing the citrate quartet, Cit(q), in the window 2.80−3.05 ppm. The lineshape normalization is made to the peak in the sub-band 2.840−2.875 ppm. This is the second tall peak on the right of the window, as clearly seen on panels (a-g). The spectra in this figure are: $m = 0$, unnormalized nonderivative lineshapes for the real part (a) as well as for the magnitude mode (b) and $1 \leq m \leq 5$, normalized derivative lineshapes (c-h). As usual, the lineshape Re(FFT) is phase-corrected and its bottom part is slightly uplifted to be positive-definite, as seen on panel (a).

Among the derivative spectra (all in the magnitude mode), those from the optimized dFFT using the FID multiplied by the adaptive power-exponential filter, the APEF, with $\alpha = 3$ in Eqs. (2) and (3), are the lineshapes for $m = 1$ (c), $m = 2$ (d), $m = 3$ (e), $m = 4$ (f) and $m = 5$ (g). The unoptimized dFFT for the FID multiplied by the time power function (no filtering) is for $m = 5$ (h).

[3] Subsequently, however, for the FIDs from Ref. [30], processed by the parametric fast Padé transform (FPT) [26], it was found that the peak widths varied from resonance to resonance. This impacts on the values of the assessed metabolite concentrations.

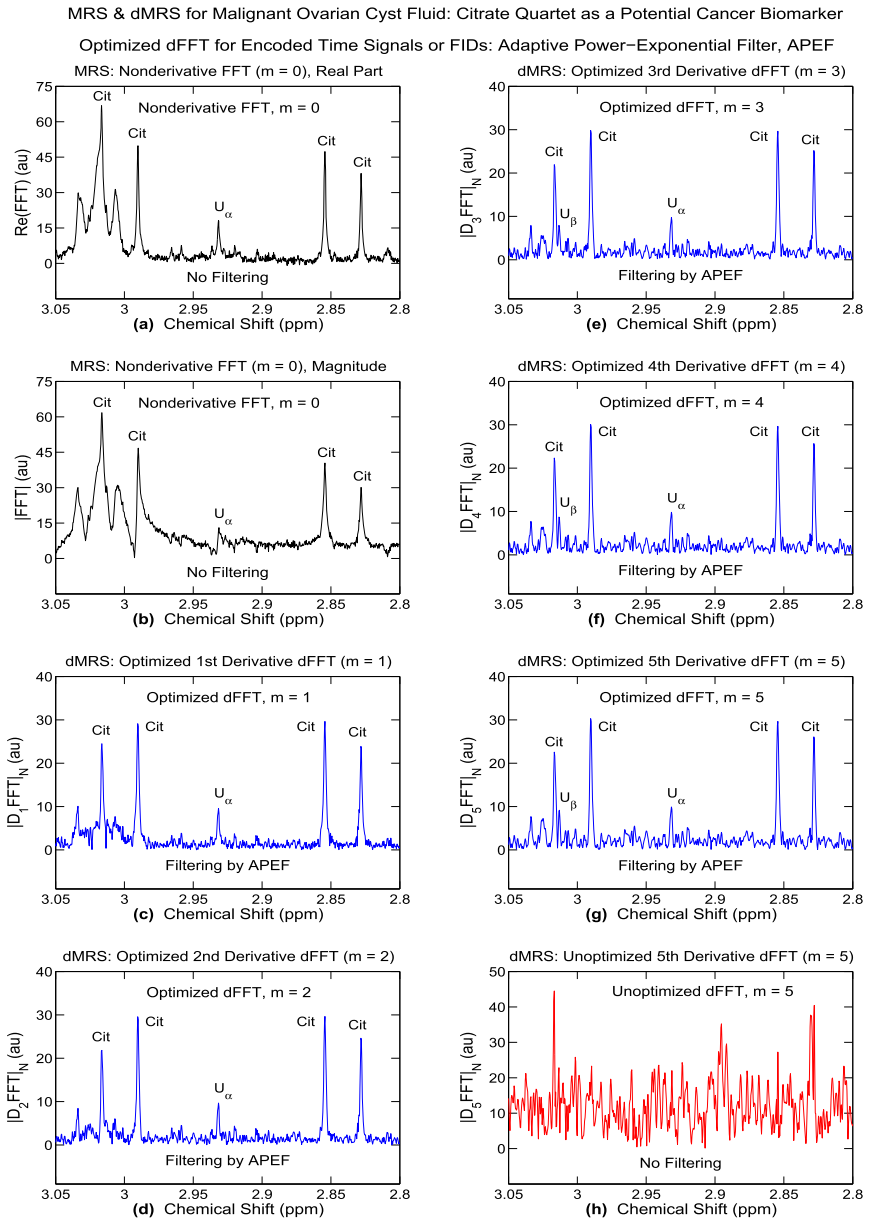


**Fig. 1** In vitro proton MRS and dMRS for samples of human biofluids: malignant ovarian cyst (serous cystadenocarcinoma) from a patient. The input time signal is the average of 128 FID transients encoded at a Bruker 600 MHz ($\approx$ 14.1T) spectrometer [30]. In a narrow band with the citrate quartet as a potential cancer biomarker for the ovary, the focus is on the derivative fast Fourier transform, the dFFT: optimized versus unoptimized. Unnormalized nonderivative FFT ($m = 0$) using (7) as: (a) Real part mode and (b) magnitude mode. Panels (c-h): normalized derivative spectra ($m = 1 - 5$) in the magnitude mode. Optimized dFFT using (1) for the APEF (2) with $\alpha = 3$ in (3): $m = 1$ (c), $m = 2$ (d), $m = 3$ (e), $m = 4$ (f) and $m = 5$ (g). Unoptimized dFFT using (7): $m = 5$ (h). The spectral intensities on the ordinates are in arbitrary units (au). Resonance frequencies (chemical shifts) on the abscissae are dimensionless units, parts per million (ppm). For details, see the text (color online)

It is seen that the real part (a) and magnitude (b) of complex nonderivative FFT spectra ($m = 0$) possess several pronounced resonances. Four of these major peaks belong to the citrate quartet, Cit(q). The centers of the four citrate peaks can roughly be read off from the graph to be located near 2.825, 2.86, 2.985 and 3.02 ppm. Herein, noise is evidently present, peak distortions are also notable and the background baseline is visibly elevated. A dominant fraction of a higher background level (a, b) stems from wider resonances that are usually assigned to heavier macromolecules (proteins, etc.).

Linearity of the nonderivative FFT ($m = 0$) brings the entire noise from the time-domain encodings to the computed frequency-domain spectra. Spectral deformations of the FFT lineshapes (a, b) are largely caused by tight overlaps of the given peak with its adjacent resonances. A marked similarity of spectra (a) and (b) is obvious, although some parts of |FFT| look more deformed than in Re(FFT). Any differences between these two lineshapes are attributed to the interference effect between Re(FFT) and Im(FFT) in the magnitude mode |FFT|. The differences are most visible for the middle sections of panels (a, b) around 2.930 ppm as well as for several inverted smaller peaks in |FFT| (b) near 2.810, 2.905, 2.925 and 2.952 ppm.

The bottom part (base) of each of the four components (partial lineshapes) of Cit(q) on panels (a, b) are broadened from distortions by the surroundings that include the background and the other unknown resonances. This is obstructive and leads to a noticeable lineshape asymmetry, especially for the two citrate peaks on the left of the whole window, close to 2.985 and 3.02 ppm (a, b). In particular, the fourth citrate peak, positioned at about 3.02 ppm, is heavily perturbed and has shoulders on both of its sides. It rides on a higher background baseline in |FFT| (b) and is significantly broader than the other three resonances of Cit(q). Moreover, its peak heights on panels (a, b) are exaggerated from constructive interferences with the two intense immediate neighboring resonances of unequal widths. Theoretically, in Cit(q), its two outer peaks should both be shorter than the two inner peaks. On panels (a, b), this holds true in the part of the window on the right (near 2.825 and 2.86 ppm), but not on the part from the left (close to 2.985 and 3.02 ppm).

Taken together, the situation seen on panels (a, b) of Fig. 1 for the nonderivative FFT ($m = 0$) is not conducive even to a rough determination of the peak area of Cit(q) as a whole nor for each of the four partial lineshapes of this quartet. Consequently, the nonderivative lineshapes in the FFT (a, b, $m = 0$) are not of use to MRS. This circumstance calls for an alternative approach to signal processing. One of the possible avenues can be tried within derivative shape estimations. For instance, two such processors could be applied, the unoptimized dFFT [25–28] and the optimized dFFT [29]. The present reconstruction results by these two methods for the citrate quartet are given on the remaining panels (c-h) of Fig. 1.

It is seen that the optimized dFFT makes a critical advance while covering the five consecutive derivative orders $1 \leq m \leq 5$ (c-g). In fact, the initial gain is obtained already with the first derivative lineshape (c, $m = 1$). Herein, the relative heights of all the four resonances from Cit(q) changed with respect to (a, b, $m = 0$). Namely, as it should be, both of the outer resonances are now lower than the inner peak pair of Cit(q). The most striking improvement for $m = 1$ (c) relative to $m = 0$ (a, b) occurs on the left of the window, around the fourth citrate peak near 3.02 ppm.

Compared to this peak, its formerly two broad neighboring resonances for $m = 0$ (a, b) are strongly suppressed for $m = 1$ (c), one slightly more than the other on account of a visibly wider breadth. Moreover, the higher derivatives $2 \leq m \leq 5$ (d-g) make in plain view steady and systematic lineshape ameliorations by the optimized dFFT. This drive proceeds unabated until all the four spectral profiles of Cit(q) ultimately attain their stabilized forms for $m = 5$ (g).

Besides the individually well-resolved four partial lineshapes of Cit(q), there are also a few unassigned spectral profiles. Some of these unknown resonances might arguably be assigned to e.g. nitrogen acetyl aspartate (NAA). Ordinarily, sizable concentrations of this neurotransmitter are detectable mainly in the brain tissues. Nevertheless, they have been found also in some other organs in the human body in lower and higher concentrations [44–53]. In Fig. 1, particular attention can be called to the unassigned (or unknown) metabolites denoted by $U_\alpha$ and $U_\beta$ near 2.930 and 3.015 ppm, respectively. However, $U_\beta$ is masked for $m = 0$ (a, b), but therein $U_\alpha$ can be spotted.

More specifically, $U_\alpha$ is well-delineated and severely deformed in Re(FFT) and |FFT| on panels (a) and (b), respectively. However, regarding particularly $U_\alpha$, what is lost in |FFT| (b), the optimized dFFT is able to recuperate already for $m = 1$ (c). Namely, the shape of $U_\alpha$ in the magnitude $|D_1\mathrm{FFT}|_\mathrm{N}$ (c, $m = 1$) looks much the same as that in the real part mode Re(FFT) on panel (a, $m = 0$). Further, for higher derivatives, the optimized dFFT is able to fully stabilize both $U_\alpha$ and $U_\beta$. They are well separated from the overcrowded baseline and delineated as two sharp peaks for $m = 4$ (f) and $m = 5$ (g).

For Cit(q), it is theoretically anticipated that the heights of the two outer peaks should be nearly the same. This is the case for $m = 1$ (c). However, for $m = 2 - 5$ (d-g), there are some departures from such an expectation. Namely, for $m = 2 - 5$ (d-g), the fourth peak of Cit(q), near 3.02 ppm, is lower than its outer counterpart, which is the citrate first peak close to 2.825 ppm. The reason is in the occurrence that the separation of the adjacent peak $U_\beta$, formerly hidden for $m = 0$ (a, b), necessarily takes away some of the intensity/power of the fourth resonance of Cit(q), lying near 3.02 ppm. As a further theoretical prescription, the heights of the two inner peaks of Cit(q), near 2.86 and 2.985 ppm, are supposed to be equal and more elevated than those of the outer two resonances at about 2.825 and 3.02 ppm. This feature is steadily maintained in the optimized dFFT for $m = 1 - 5$ (c-g).

Relative to the nonderivative FFT (a, b, $m = 0$), the achievements of the optimized dFFT (c-g, $m = 1 - 5$) in Fig. 1 are remarkable. Such an outcome is possible because of the chief tandem advantage of this processor: higher resolution and enhanced SNR. More concretely, by the optimized dFFT, the background baseline is considerably lowered in the entire Nyquist interval, including the window 2.80−3.05 ppm, with the implication of noise reduction. Moreover, the citrate quartet resonances are narrowed and this in itself yields a higher resolution.

Thus, for $m = 1 - 5$ (c-g) in Fig. 1, the optimized dFFT realizes the principal goal of a proper derivative estimation. This goal consists of extracting the sought information with more physical content and less noise than what is offered by the nonderivative FFT (a, b, $m = 0$). The attractiveness of such an accomplishment is in the fact that no fitting whatsoever is used to reconstruct the four components (readily

quantifiable by the peak integrations) of the exemplified multiplet, the citrate quartet, Cit(q). Moreover, no model either is used for the FID waveform nor for the shape of the peaks.

This conclusion is a stark contradistinction to the associated predictions by the unoptimized dFFT for $m = 5$ (h). Herein, no physical information is contained since noise prevails totally. The reason is that for encoded FIDs, noise dominates at larger times $t$ in the product $t^m c(t)$, processed by the unoptimized dFFT. Moreover, as opposed to panel (g), it is observed that the derivative-induced noise lifts the background baseline on panel (h). Thus, without optimization by the APEF, noise offsets the theoretically anticipated advantage of derivative estimations. In the end, the unoptimized dFFT (h, $m = 5$) becomes much worse than even the already poor nonderivative FFT (a, b, $m = 0$).

As explained in Sect. 2, the unavoidable truncations of the encoded $c(t)$ or FIDs at a finite total acquisition time ($T < \infty$) yield the Gibbs ringing deformations in the corresponding spectra from the nonderivative FFT ($m = 0$). Such spectral artifacts, on top of the already existing distortions due to the inherently noisy tails of the encoded FID, become exacerbated in the processed product $t^m c(t)$ for the increased derivative order $m$. Consequently, function $t^m c(t)$ is ill-conditioned and leads to divergence, which is induced by the monomial $t^m$. This causes the unoptimized dFFT to fail flagrantly, as seen for $m = 5$ (h).

Of course, the same obstacle with $t^m c(t)$ is also shared by the optimized dFFT. However, this latter processor is capable of regularizing (countering) the detrimental effect of $t^m$. Namely, in the optimized dFFT, the tempering feature of the regularization effect of the APEF on the offending power function $t^m$ yields the well-behaved, converging spectral lineshapes that are especially solidified for $m = 3 - 5$ (e-g).

### 3.2 Three singlets of the choline compound (3.17−3.29 ppm)

For malignancy diagnostic detection by means of MRS of critical importance are molecules of cholines as recognized cancer biomarkers for several organs (brain, breast, prostate, ovary). Choline compounds are comprised of three singlets, free choline Cho(s), phosphocholine PCho(s), or PC(s) for short, and glycerophosphocholine GPC(s). Besides the Cho, PC and GPC components of total choline (tCho), the metabolite map in Fig. 2 also shows several other resonances, such as taurine (Tau), phosphoethanolamine (PE), $\beta-$glucose ($\beta-$Glc) and myo-inositol (m-Ins).

The main attention in Fig. 2 is placed onto free choline Cho(s). The reason is in the intriguing reconstructions by the derivative fast Padé transform (dFPT) using its two variants, nonparametric [25] and parametric [26]. In Ref. [25], it seemed at first that a resonance, which is usually assigned to free choline, was a 'doubtless' singlet in the nonparametric nonderivative fast Padé transform, the FPT. Then, using the nonparametric dFPT, that apparent 'singlet' was found in the same study [25] to be an amalgamate of two fully isolated peaks.

Such an intriguing splitting has subsequently been confirmed by the parametric dFPT [26]. These genuine singlets were lying in their close mutual proximity, on each side of 3.19 ppm, which is customarily considered as the resonance frequency of

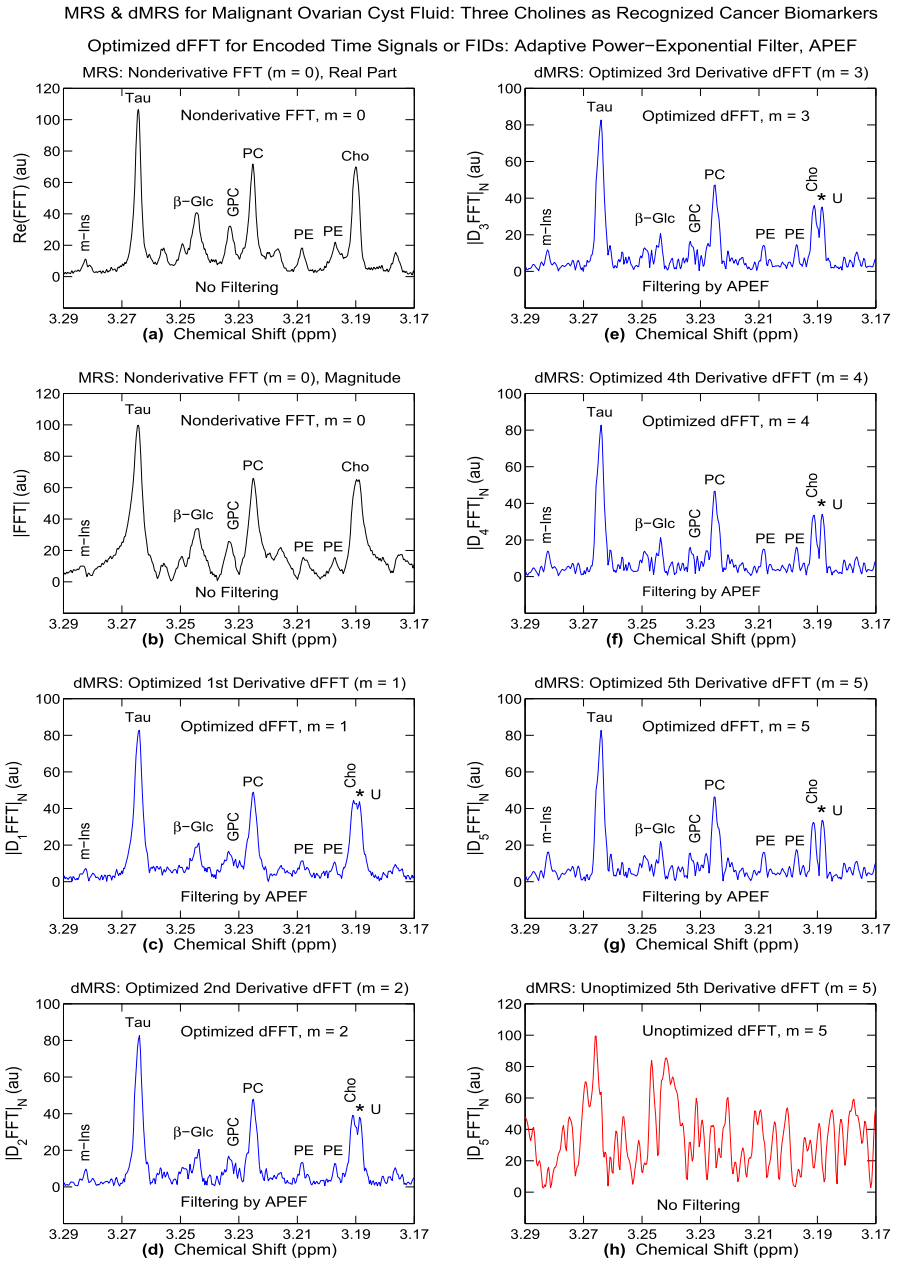


**Fig. 2** In vitro proton MRS and dMRS for samples of human biofluids: malignant ovarian cyst (serous cystadenocarcinoma) from a patient. The input time signal is the average of 128 FID transients encoded at a Bruker 600 MHz ($\approx$ 14.1T) spectrometer [30]. In a narrow band with the choline compounds as recognized cancer biomarkers for the ovary, the focus is on the derivative fast Fourier transform, the dFFT: optimized versus unoptimized. Unnormalized nonderivative FFT ($m = 0$) using (7) as: (a) Real part mode and (b) magnitude mode. Panels (c-h): normalized derivative spectra ($m = 1 - 5$) in the magnitude mode. Optimized dFFT using (1) for the APEF (2) with $\alpha = 3$ in (3): $m = 1$ (c), $m = 2$ (d), $m = 3$ (e), $m = 4$ (f) and $m = 5$ (g). Unoptimized dFFT using (7): $m = 5$ (h). The spectral intensities on the ordinates are in arbitrary units (au). Resonance frequencies (chemical shifts) on the abscissae are dimensionless units, parts per million (ppm). For details, see the text (color online)

Cho(s) itself. Both these singlets were baseline-resolved, one of them was assigned to Cho(s) while the other was left unassigned and provisionally denoted by U(s) in Refs. [25, 26]. The latter resonance was missed by the nonderivative FFT in Ref. [30].

Here, the clause 'baseline-resolved' refers to a circumstance where the given overlapped spectral compound is split apart into its two or more hidden constituents down to the low-lying background baseline, which is itself near the chemical shift axis. We want to find out whether in the optimized dFFT, the free choline resonance could likewise exhibit a shoulder, which might ultimately escape its tight overlap with Cho(s) and stabilize as a separate unknown peak U(s) for increasing derivative orders $m$. Such a clustering of Cho(s) is important to clarify (confirm or disprove) by means of another shape estimator different from the nonparametric dFPT [25], e.g. by the optimized dFFT. Obviously, the concentration [tCho] of tCho, given by [tCho]=[Cho(s)]+[PC(s)]+[GPC(s)], can be reliably assessed only if the three abundance levels [Cho(s)], [PC(s)] and [GPC(s)] have been accurately estimated first.

In Fig. 2, the nonderivative spectrum ($m = 0$) is shown in two representations, the real part Re(FFT) and the magnitude |FFT| of complex FFT, on panels (a) and (b), respectively. The spectrum Re(FFT) on panel (a) is positive-definite, which is achieved by a phase correction and a slight uplifting of the bottom part of this lineshape. These two adjustments are the same as those mentioned with Fig. 1.

All the magnitude-mode derivative spectra $|\mathrm{D}_m\mathrm{FFT}|_\mathrm{N}$ ($m > 0$) are on the remaining panels (c-h, $m = 1 - 5$) of this figure. Thus, the optimized dFFT, with the FID multiplied by the adaptive power-exponential filter, the APEF, with $\alpha = 3$ in Eqs. (2) and (3), is for $m = 1$ (c), $m = 2$ (d), $m = 3$ (e), $m = 4$ (f) and $m = 5$ (g). The unoptimized dFFT (no filtering) with the FID multiplied by the time power function is for $m = 5$ (h). Panels (a-g) clearly exhibit a set of several pronounced resonances, some of which are assigned to the mentioned known metabolites, e.g. Cho, PE, PC, GPC, $\beta-$Glc, Tau and m-Ins.

Peaks related to these molecules are seen to be superimposed on an elevated background baseline in |FFT| (b, $m = 0$) with their broadened bases. The broadening factor in |FFT|, seen in the full width at half maximum (FWHM), is approximately equal to $\sqrt{3}$ relative to Re(FFT) on panel (a, $m = 0$). In fact, for a synthesized noiseless FID, yielding a pure Lorentzian absorption with a true single resonance peak, the FWHM for |FFT| is wider than that for Re(FFT) by a factor which is $\sqrt{3}$ exactly [17]. However, a departure from the $\sqrt{3}$ scaling may occur for an encoded FID which, due to its nonzero phase, yields a mixture of Re(FFT) and the imaginary part Im(FFT) in both the 'absorption' and 'dispersion' modes [54].

The lineshapes of the peaks in Fig. 2 are more symmetric in Re(FFT) on panel (a) than in |FFT| on panel (b). Even with excellent static magnet shimming [30], there are still several reasons for a visible skewness of the magnitude spectrum for $m = 0$ (b). One reason is the mentioned interference between Re(FFT) and Im(FFT) in the magnitude |FFT|. Another reason is a realistic possibility for the existence of one or more hidden resonances [27].

A huge number of molecules take part in the successive stages of various metabolisms in cells of human organs. Despite their different structures, many of these metabolites still share a common feature: similar values of their transverse relaxation times $T_2^\star$. Such an occurrence is the main cause for the abundantly encountered over-

laps among adjacent resonances in NMR spectra (the mentioned "spectral crowding" [30–35]). This extends throughout the Nyquist range, even at high magnetic field strengths, such as 14.1T considered presently as well as in Refs. [25–27, 30, 55] and elsewhere.

A near-symmetry of some of the 'absorptive' spectral profiles, such as that of free choline in Re(FFT) on panel (a), has been assumed in Ref. [30] to be sufficient for quantification. This is tenuous for 'determining' the peak area (and, hence, the related metabolite concentration) by either integration or fitting the lineshapes to some prescribed mathematical forms. Using a numerical integration for an 'absorption' would lead to errors whenever the integration limits cannot be assessed properly, as in Re(FFT) on panel (a).

Moreover, fitting the presumed partial lines by e.g. Lorentzians [30], is also risky. The reason is that an arbitrary number of unequal Lorentzians with sharply varying adjustable parameters might yield the practically indistinguishable summed lineshape. Then, this too is hardly the way to proceed in trying to resolve the given overlap into its true components.

An alternative is offered by the optimized dFFT, which has been shown to provide the reliable component spectra, reconstructed from FIDs encoded by in vitro MRS at widely different magnetic field strengths (1.5, 14.1T) [29]. This quantification-able estimator is nonparametric because no model function is invoked for either the encoded FID nor for the corresponding retrieved spectral lineshapes. It can safely exploit the higher derivatives ($m \leq 6$ [29]), thanks to the derivative-adapted optimization. A set of spectra of the like derivative orders $1 \leq m \leq 5$ is also presented in Fig. 2. Therein, even a cursory look would reveal a steady improvement of reconstructions by the optimized dFFT for $m = 1 - 5$ (c-g).

A marked trend of this progress begins to settle in already with $m = 1$ (c). The background baseline, which is noticeably high for $m = 0$ (b), is brought down for $m = 1$ (c) and is observed to lie close to the chemical shift axis. Recall that, by definition, the nonderivative FFT (a, b, $m = 0$) is based on integrating the given FID in the time interval $t \in [0, T]$ by way of the Riemann sum in (6) with discretized $t$ and $\nu$. However, every integration acts as a smoothing operator because it is a weighted average of the function to be integrated.

That is why most of the weak spectral structures piled up on the tails of the individual peaks in the nonderivative FFT (a, b, $m = 0$) are barely noticeable. Conversely, the derivative operator $\mathrm{D}_m = (\mathrm{d}/\mathrm{d}\nu)^m$ is an anti-smoothing operator, which acts as a deconvolving/unfolding operator. As such, what was smoothed out by the nonderivative FFT (a, b, $m = 0$), is partially unsmoothed/unsmeared by the optimized dFFT (c, $m = 1$). As a consequence, the mentioned weaker spectral structures in the nonderivative FFT (a, b, $m = 0$) become unfolded and more or less sharply propelled in the first derivative (c, $m = 1$) of the optimized dFFT.

Ideally, using a theoretical noiseless FID, synthesized for only one metabolite, giving a perfect complex Lorentzian spectrum, its pure nonderivative absorption ($m = 0$) and the corresponding first derivative magnitude ($m = 1$) have the identical FWHM [17]. On the other hand, all FIDs encoded by in vitro and/or in vivo MRS from human biofluids or tissues are noisy and they lead to nonderivative multi-component complex-valued lineshapes.

As emphasized, these complex-valued resonance profiles contain the mixtures of 'absorptions' and 'dispersions' in both the real and imaginary parts of the spectra [54]. Nevertheless, despite such deviations from spectra employing simulated time signals, the lineshapes of a nonderivative 'absorption' ($m = 0$) and the corresponding first derivative ($m = 1$) magnitude mode for encoded FIDs could still have quite similar values for their FWHM.

It is then tempting to say that a failure to abide by this rule could serve as an indication of the presence of one or more invisible resonances beneath a peak, ordinarily viewed as a singlet resonance. However, even if this theoretical prediction is duly confirmed for encoded FIDs, e.g. an apparent singlet may nevertheless contain some hidden peaks. Regarding Fig. 2 in this context, by superimposing $|\mathrm{D}_1\mathrm{FFT}|_\mathrm{N}$ (c, $m = 1$) on Re(FFT) from panel (a, $m = 0$), one would observe practically the same FWHM for one of the three major peaks taken at a time (be it Cho, PC or Tau).

Still, this does not imply that the almost symmetric lineshape of e.g. Cho in Re(FFT) on panel (a, $m = 0$) does not contain an invisible tightly glued neighboring resonance. Quite the contrary, the peak close to the expected location of Cho(s) begins to fragment on its top/summit positioned at 3.19 ppm already in $|\mathrm{D}_1\mathrm{FFT}|_\mathrm{N}$ (c, $m = 1$). This splitting only becomes deeper with the gradually augmented derivative orders, as is clear from $|\mathrm{D}_m\mathrm{FFT}|_\mathrm{N}$ for $m = 2 - 5$ (d-g).

With the progression in the ability of $|\mathrm{D}_m\mathrm{FFT}|_\mathrm{N}$ ($m > 1$) from the optimized dFFT to extract a separate well-delineated resonance, eventually the unknown/unassigned singlet U(s) becomes stabilized for $m = 5$ (g). Such a happening takes place extremely close to 3.19 ppm, where the resonance lineshape in Re(FFT) on panel (a, $m = 0$) indicates no summation of the type, Cho(s)+U(s). However, when this compound is described with |FFT| (b, $m = 0$), a slight notching can be noticed by zooming near the splitting frequency (3.19 ppm).

Overall, then, independently of the nonparametric dFPT [25], by way of $|\mathrm{D}_m\mathrm{FFT}|_\mathrm{N}$ (g, $m = 5$), the optimized dFFT also unequivocally detects U(s). It is seen for $m = 5$ (g) that the two separate resonances Cho(s) and U(s) are of basically the same strength/intensity. Thus, the usage of Re(FFT) from panel (a) to roughly estimate the peak area of free choline, considered as a lone singlet near 3.19 ppm, implies that the obtained result would be overestimated by a factor of 2.

This would, in turn, invalidate the concentration [Cho(s)] and that of [tCho] due to the mentioned relation [tCho]=[Cho(s)]+[PC(s)]+[GPC(s)]. Moreover, it would also be guess-work to try to complete the expression for [tCho] with an estimate for [PC(s)], based on the peak area of phosphocholine on panel (a, $m = 0$) in Re(FFT). Therein, the PC resonance too looks like a single quite symmetric peak. However, this appearance is faded away already for $m = 1$ (c), where the PC resonance acquires a left-hand-side bulge, which for $m = 2 - 5$ (c-g) becomes an isolated peak. This takes away some of the power of PC(s). Moreover, the right-hand-side shoulder in the PC resonance for $m = 4$ (f) and $m = 5$ (g) also becomes a separate peak, as we explicitly checked for $m > 6$.

The moral of this story is that every peak in a spectrum reconstructed by any nonderivative shape estimator, including the FFT, using encoded FIDs should be treated as a potential multiplet. To rule out the possible composite structure of singlet-appearing peaks, e.g. the optimized dFFT can be applied.

As to the unoptimized dFFT, panel (h, $m = 5$) shows that no meaningful information whatsoever remains at the fifth derivative. Therein, the derivative-enhanced noise completely overwhelms the physical content, which becomes unrecognizable. This deterioration is illustrated on panel (h) for the fifth derivative, but it also occurs at the lower derivatives with orders $m = 2-4$ (not shown to avoid clutter). Overall, similarly to the outcome of the analysis of the citrates, the conclusion for the cholines in Fig. 2 is also that the Fourier-based derivative signal processing absolutely necessitates a properly adapted optimization, such as that provided by the APEF, which is used in the optimized dFFT.

## 4 Conclusions

An upgrade of the Fourier analysis is reported, as it applies to the wide field of signal processing with the myriad of settings, including the medical applications in tumor diagnostics by magnetic resonances spectroscopy (MRS). This is an advance achieved simultaneously in improved frequency resolution and signal-to-noise ratio (SNR). The main two advantages of the standard fast Fourier transform (FFT) are its model-independence and a high computational expedience of the Cooley-Tukey algorithm [1]. No mathematical forms for either the encoded free induction decay (FID) data or the lineshapes in the spectra are employed.

On the other hand, there are several notable disadvantages of the FFT. Resolution is low (proportional to the reciprocal of the FID length) and SNR is poor. Due to the linearity feature of the FFT, the entire noise (without any suppression whatsoever) from encoded FIDs is brought to the computed spectra. The stumbling block in shape estimations by the FFT is its inability to split apart the overlapped peaks that are abundantly present in spectra for encoded FIDs. Such problems of the FFT are not solved in a satisfactory manner by the customary digital filters because they may improve resolution or SNR, but not both.

Still, simultaneous enhancement of resolution and SNR should be achievable by derivative signal processing. Yet, this has not met with success in the unfiltered derivative fast Fourier transform (dFFT). This method, applied to encoded FIDs, catastrophically worsens both resolution and SNR (even relative to the FFT), already above the second derivative. However, the second derivatives are insufficient for resolving the tightly overlapped peaks. The reason for the failure of the unfiltered dFFT is in the unattenuated time power function (monomial), which multiplies the encoded FID. This monomial (resulting from applying the frequency derivative operator to the FFT), weighs heavily the noise-dominated tail of encoded FIDs.

Nevertheless, a recent optimization of the Fourier-based derivative signal processing comes to the rescue [29]. This newest advance utilizes the critically important derivative-adapted damped exponential or Gaussian filters capable of surmounting the mentioned stumbling block while improving both resolution and SNR. The resulting estimator, called the optimized dFFT, exhibits an outstanding performance in versatile applications.

The presently reported illustrations are concerned with the FIDs encoded from samples of human malignant ovarian cyst fluid by using in vitro MRS at a 600 MW

(14.1 MHz) Bruker spectrometer. The spectra reconstructed by the optimized dFFT are of very high quality. The overlapped peaks are separated and, as such, not only clearly visualized, but also amenable to reliable quantification. Such characteristics are deemed to be invaluable when dealing with the patient data encoded also by in vivo MRS. This emerging advance in signal processing would allow directly the physician to interpret the quantitative reconstructions of utmost diagnostic relevance and thus help decision making.

**Acknowledgements** The authors thank the 'Radiumhemmet Research Fund' at the Karolinska University Hospital, the 'Fund for Research, Development & Education (FoUU) of the Stockholm County Council' and the 'Fund from the Marsha Rivkin Center for Ovarian Cancer Research in Seattle, USA'. Open Access has been provided by the Karolinska Institute, Stockholm, Sweden. We would like to thank our colleagues, Professors Marinette van der Graaf, Leon Massuger, Ron Wevers, Eva Kolwijck, Udo Engelke, Arend Heerschap, Henk Blom, M'Hamed Hadfoune, and Wim A. Buurman from Radboud University in Nijmegen, The Netherlands, for kindly allowing us to use one of the in vitro time signals that they have encoded and reported in Ref. [30].

**Author contributions** Signal processing and the art work have been carried by DžB. Analysis of the obtained spectra has been performed by DžB and KB. Both authors cooperatively designed this study and critically read as well as approved the final version of the manuscript submitted for publication.

**Funding** Open access funding provided by Karolinska Institute. Open access funding provided by the Karolinska Institute. This work is funded by the Radiumhemmet Research Funds, King Gustaf the Fifth Jubilee Fund at the Karolinska University Hospital, Fund for Research, Development and Education (FoUU) of the Stockholm County Council.

**Data Availability Statement** Data from this work can be made available to other researchers in this field upon request to the Authors.

## Declarations

**Conflict of interest** The Authors have no competing interests.

**Ethical approval** The Regional Ethics Committee, Karolinska Institute, Stockholm (DNR # 708-31/1, Protocol 20-06-2007) found no ethical issues that would preclude carrying out this work.



## References

1. J.W. Cooley, J.W. Tukey, An algorithm for machine calculation of complex Fourier series. Math. Comp. 19, 297–301 (1965)
2. J.C. Lindon, A.G. Ferrig, Digitisation and data processing in Fourier transform NMR. Progr. NMR Spectr. 14, 27–66 (1989)
3. B. Porat, A Course in Digital Signal Processing (John Wiley & Sons Inc., New York, 1997)
4. R.N. Bracewell, The Fourier Transform and Its Applications. 3rd edn. (McGraw-Hill, New York, 2000)

5. R.E. Ernst, W.A. Anderson, Application of Fourier transform spectroscopy to magnetic resonance. Rev. Sci. Instrum. 37, 93–102 (1966)
6. R.E. Ernst, Sensitivity enhancement in magnetic resonance. Adv. Magn. Reson. 2, 1–135 (1966)
7. B. Maraviglia, ed. Magnetic Resonance and Brain Function: Approaches from Physics (IOS Press, Amsterdam, 1999)
8. L.A. Brandão, R.C. Dominges, MR Spectroscopy of the Brain. (Lippincott Williams & Wilkins, Philadelphia, UK 2004)
9. K.V. Chary, G. Govil, NMR in Biological Systems: from Molecules to Humans (Springer, Dordrecht, The Netherlands, 2008)
10. Dž. Belkić, *Quantum-Mechanical Signal Processing and Spectral Analysis* (Taylor & Francis via CRC Press, London, 2005)
11. Dž. Belkić, K. Belkić, *Signal Processing in Magnetic Resonance Spectroscopy with Biomedical Applications* (Taylor & Francis via CRC Press, London, 2010)
12. Dž. Belkić, K. Belkić, eds. Magnetic Resonance Imaging and Spectroscopy, Vol. 3 in Comprehensive Biomedical Physics (Elsevier, Amsterdam, 2014)
13. I.C.P. Smith, R. Baert, Medical diagnosis by high resolution NMR of human specimens. IUBMB Life **55**, 273–277 (2003). ([IUBMB: International Union of Biochemistry and Molecular Biology])
14. U. Sharma, N. Jagannathan, Metabolism of prostate cancer by magnetic resonance spectroscopy (MRS). Biophys. Rev. 12, 1163–1173 (2020)
15. Dž. Belkić, K. Belkić, Exact quantification by the nonparametric fast Padé transform using only shape estimation of high-order derivatives of envelopes. J. Math. Chem. **56**, 268–314 (2018)
16. Dž. Belkić, K. Belkić, Explicit extraction of absorption peak positions, widths and heights using higher order derivatives of total shape spectra by nonparametric processing of time signals as complex damped multi-exponentials. J. Math. Chem. **56**, 932–977 (2018)
17. Dž. Belkić, K. Belkić, Validation of reconstructed component spectra from non-parametric derivative envelopes: comparison with component lineshapes from parametric derivative estimations with the solved quantification problem. J. Math. Chem. **56**, 2537–2578 (2018)
18. Dž. Belkić, K. Belkić, Review of recent applications of the conventional and derivative fast Padé transform for magnetic resonance spectroscopy. J. Math. Chem. **57**, 385–464 (2019)
19. Dž. Belkić, K. Belkić, Feasibility study for applying the lower-order derivative fast Padé transform to measured time signals. J. Math. Chem. **58**, 146–177 (2020)
20. Dž. Belkić, K. Belkić, Derivative NMR spectroscopy for J-coupled multiplet resonances with short time signals (0.5KB) encoded at low magnetic field strengths (1.5T): I. Part. Water Suppressed. J. Math. Chem. **59**, 364–404 (2021)
21. Dž. Belkić, K. Belkić, Derivative NMR spectroscopy for J-coupled multiplet resonances with short time signals (0.5KB) encoded at low magnetic field strengths (1.5T): I.I. Part. Water Unsuppressed. J. Math. Chem. **59**, 405–443 (2021)
22. Dž. Belkić, K. Belkić, In vivo derivative NMR spectroscopy for simultaneous improvements of resolution and signal-to-noise-ratio: Case study. Glioma. J. Math. Chem. **59**, 2133–2178 (2021)
23. Dž. Belkić, K. Belkić, Exact quantification by shape estimations, High-resolution at 3T for in vivo derivative NMR spectroscopy in medical diagnostics of ovarian tumor. J. Math. Chem. **59**, 2218–2260 (2021)
24. Dž. Belkić, K. Belkić, Derivative NMR spectroscopy for J-coupled resonances in analytical chemistry and medical diagnostics. Adv. Quantum Chem. **84**, 95–265 (2021)
25. Dž. Belkić, K. Belkić, In vitro proton magnetic resonance spectroscopy at 14T for benign and malignant ovary: Part I, Signal processing by the nonparametric fast Padé transform. J. Math. Chem. **60**, 373–416 (2022)
26. Dž. Belkić, K. Belkić, In vitro proton magnetic resonance spectroscopy at 14T for benign and malignant ovary: Part II, Signal processing by the parametric fast Padé transform. J. Math. Chem. **60**, 1200–1271 (2022)
27. Dž. Belkić, K. Belkić, Magnetic resonance spectroscopy at high magnetic fields: Derivative reconstructions of components from envelopes using encoded time signals. Adv. Quantum Chem. **86**, 151–221 (2022)
28. Dž. Belkić, K. Belkić, Inverse problem for reconstruction of components from derivative envelope in ovarian MRS: Citrate quartet as a cancer biomarker with considerably decreased levels in malignant vs benign samples. J. Math. Chem. **61**, 569–599 (2023)

29. Dž. Belkić, K. Belkić, Derivative shape estimations with resolved overlapped peaks and reduced noise for time signals encoded by NMR spectroscopy with and without water suppression. J. Math. Chem. **61**, 1936–1966 (2023)
30. E.A. Boss, S.H. Moolenaar, L.F. Massuger, H. Boonstra, U.F. Engelke, J.G. de Jong, R.A. Wevers, High-resolution proton nuclear magnetic resonance spectroscopy of ovarian cyst fluid. NMR Biomed. 13, 297–305 (2000)
31. J.K. Nicholson, I.D. Wilson, High resolution proton magnetic resonance spectroscopy of biological fluids. Progr. NMR Spectr. 21, 449–501 (1989)
32. M.E. Yacoe, G. Sommer, D. Peehl, In vitro proton spectroscopy of normal and abnormal prostate. Magn. Reson. Med. 19, 429–438 (1991)
33. B. Liang, L.K. Tamm, NMR as a tool to investigate membrane protein structure, dynamics and function. Nat. Struct. Mol. Biol. 23, 468–474 (2016)
34. S. Perez Santero, F. Favretto, S. Zanzoni, R. Chignola, M. Assfalg, M. D'Onofrio (2016) Effects of macromolecular crowding on a small lipid binding protein probed at the single-amino acid level. Arch. Biochem. Biophysics 606, 99–110
35. Dž. Belkić, K. Belkić, In vivo magnetic resonance spectroscopy for ovarian cancer diagnostics: quantification by the fast Padé transform. J. Math. Chem. **55**, 349–405 (2017)
36. M. Kyriakides, N. Rama, J. Sidhu, H. Gabra, H.C. Keun, M. El-Bahrawy, Metabonomic analysis of ovarian tumour cyst fluid by proton nuclear magnetic resonance spectroscopy. Oncotarget 7, 7216–7226 (2016)
37. J. Kurhanewicz, R. Dahiya, J.M. Macdonald, L.-H. Chang, T.L. James, P. Narayan, Citrate alterations in primary and metastatic human prostatic adenocarcinomas: $^{1}$H magnetic resonance spectroscopy and biochemical study. Magn. Reson. Med. **29**, 149–157 (1993)
38. J. Kurhanewicz, D.B. Vigneron, S.J. Nelson, H. Hričak, J.M. McDonald, B. Konety, P. Narayan, Citrate as an in vivo marker to discriminate prostate cancer from benign hyperplasia and normal prostate peripheral zone: Detection via localized proton spectroscopy. Urology, 45, 459–466 (1995)
39. A. Meumlemans, Editorial comment (on Ref. [38]). Urology, **45**, 466 (1995)
40. M.G. Swanson, D.B. Vigneron, Z.L. Tabatabai, J. Simko, S. Jarso, K.R. Keshari, L. Schmitt, P.R. Carrol, K. Shinohara, J. Kurhanewicz, Proton HRMAS spectroscopy and quantitative pathologic analysis of MRI/3D MRSI targeted postsurgical prostate tissues. Magn. Reson. Med. 50, 944–954 (2003)
41. M.G. Swanson, K.R. Keshari, Z.L. Tabatabai, J.P. Simko, K. Shinohara, P.R. Carrol, A.S. Zektzer, J. Kurhanewicz, Quantitative analysis of prostate metabolites using $^{1}$H HRMAS spectroscopy. Magn. Reson. Med. 55, 1257–1264 (2006)
42. M.G. Swanson, K.R. Keshari, Z.L. Tabatabai, J.P. Simko, K. Shinohara, P.R. Carrol, A.S. Zektzer, J. Kurhanewicz, Quantification of choline and ethanolamine-containing metabolites in human prostate tissue using $^{1}$H HRMAS total correlation spectroscopy. Magn. Reson. Med. 60, 33–40 (2008)
43. M.B. Tessem, M.G. Swanson, K.R. Keshari, M.J. Albers, D. Joun, Z.L. Tabatabai, J.P. Simko, K. Shinohara, S.J. Nelson, D.B. Vigneron, I.S. Gribbestad, J. Kurhanewicz, Evaluation of lactate and alanine as metabolite biomarkers of prostate cancer using $^{1}$H HRMAS spectroscopy of biopsy tissue. Magn. Reson. Med. 60, 510–516 (2008)
44. M.H. Baslow, S. Yamada, Identification of N-acetylaspartate in the lens of the vertebrate eye: A new model for the investigation of the function of N-acetylated amino acids in vertebrates. Exp. Eye Res. 64, 283–286 (1997)
45. A.P. Burlina, V. Ferrari, L. Facci, S.D. Skaper, S.B. Burlina, Mast cells contain large quantities of secretagogue-sensitive N-acetylaspartate. J. Neurochem. 69, 1314–1317 (1997)
46. M.H. Baslow, N-acetylaspartate in the vertebrate brain: Metabolism and function. Neurochem. Res. 28, 941–953 (2003)
47. S.H. Moolenaar, U.F.H. Engelke, S.M.G.C. Hoenderop, A.C. Sewell, L. Wagner, R.A. Wevers, Bruker Handbook of $^{1}$H – NMR Spectroscopy in Inborn Errors of Metabolism. G.A. Webb, ed. (SPS Verlagsgesellschaft, Heilbronn, 2002)
48. E. Kolwijck, U.F. Engelke, M. van der Graaf, A. Heerschap, J. Henk, H.J. Blom, M. Hadfoune, W.A. Buurman, L.F. Massuger, R.A. Wevers, N-acetyl resonances in in vivo and in vitro NMR spectroscopy of cystic ovarian tumors. NMR Biomed. 22, 1093–1099 (2009)
49. E. Kolwijck, R.A. Wevers, U.F. Engelke, J. Woudenberg, J. Bulten, H.J. Blom, L.F.A.G. Massuger, Ovarian cyst fluid of serous ovarian tumors contains large quantities of the brain amino acid N-acetylaspartate. PLoS One 5, e10293 (2010)

50. M.Y. Fong, J. McDunn, S.S. Kakar, Identification of metabolites in the normal ovary and their transformation in primary and metastatic ovarian cancer. PLoS One 6, e19963 (2011)
51. D. Ben Sellem, K. Elbayed, A. Neuville, F.-M. Moussallieh, G. Lang-Averous, M. Piotto, J.-P. Bellocq, I.J. Namer (2011) Metabolomic characterization of ovarian epithelial carcinomas by HRMAS-NMR spectroscopy. J. Oncology 2011, 174019
52. B. Zand, Altered ovarian cancer metabolism increases neuronal N-acetylaspartate to promote tumor growth. UT GSBS Dissertations and Theses, Open Access. Paper 378 (2013) [UT GSBS: University of Texas, Graduate School of Biomedical Sciences], http://digitalcommons.library.tmc.edu/utgsbs_-dissertations/378/
53. B. Zand, R.A. Previs, N.M. Zacharias, R. Rupaimoole, T. Mitamura, A. Sidalaghatta Nagaraja, M. Guindani, H.J. Dalton, L. Yang, J. Baddour, A. Achreja, Wei Hu, C.V. Pecot, C. Ivan, S.Y. Wu, C.R. McCullough, K.M. Gharpure, E. Shoshan, S. Pradeep, L.S. Mangala, C. Rodriguez-Aguayo, Y. Wang, A.M. Nick, M.A. Davies, G. Armaiz-Pena, J. Liu, S.K. Lutgendorf, K.A. Baggerly, M. Bar Eli, G. Lopez-Berestein, D. Nagrath, P.K. Bhattacharya, A.K. Sood. Role of increased N-Acetylaspartate levels in cancer. J. Natl. Cancer Inst. **108**, djv426 (2016)
54. D.J. Drost, W.R. Riddle, G.D. Clarke, Proton magnetic resonance spectroscopy in the brain: Report of AAPM MR Task Group # 9. Med. Phys. **29**, 2177–2197 (2002). ([AAPM: American Association of Physicists in Medicine])
55. B. Sitter, T. Bathen, B. Hagen, C. Arentz, F.E. Skjeldestad, I.S. Gribbestad, Cervical cancer tissue characterized by high-resolution magic angle spinning MR spectroscopy. Magn. Res. Mater. Phys. Biol. Med. 16, 174–181 (2004)